

Spectral dependence of the third-order optical susceptibility of Au nanostructures: Experiments and first-principles calculations

Boyi Zhang,^{1,2,*} Rodrigo Sato,² Hiroyoshi Momida,³ Takahisa Ohno,⁴ Mykhailo Chundak,⁵ Masanobu Naito,^{6,7} Michiko Yoshitake,⁵ and Yoshihiko Takeda^{1,2,†}

¹*School of Pure and Applied Sciences, University of Tsukuba, Tsukuba, Ibaraki 305-8577, Japan*

²*Center for Green Research on Energy and Environmental Materials, National Institute for Materials Science, Tsukuba, Ibaraki 305-0003, Japan*

³*Institute of Scientific and Industrial Research, Osaka University, Osaka 567-0047, Japan*

⁴*Global Research Center for Environment and Energy based on Nanomaterials Science, National Institute for Materials Science, Tsukuba Ibaraki 305-0044, Japan*

⁵*International Center for Materials Nanoarchitectonics, National Institute for Materials Science, Tsukuba, Ibaraki 305-0044, Japan*

⁶*Research Center for Structural Materials, National Institute for Materials Science, Tsukuba, Ibaraki 305-0047, Japan*

⁷*Graduate School of Frontier Sciences, The University of Tokyo, Kashiwa, Chiba 277-8561, Japan*



(Received 12 December 2018; published 30 July 2019)

The surface plasmon resonances of Au nanoparticles have attracted wide interest for the promising functionalities in nonlinear plasmonics and nanophotonics in recent decades. However, the third-order susceptibility $\chi^{(3)}$ of Au nanostructures, one of the crucial parameters to describe the nonlinear optical properties, had been experimentally described at only a few wavelengths. These fragmental results have precluded the understanding of the physical origins. Here, we have evaluated the real and imaginary components of $\chi^{(3)}$ in a broad range (1.50–3.10 eV) through a combined analysis of spectroscopic ellipsometry and pump-probe spectroscopy. The results show that the macroscopic and intrinsic $\chi^{(3)}$ are strongly wavelength dependent and consist of several successive peaks. Furthermore, by analyzing and comparing the Au thin film to nanoparticles, the contributions of the interband and intraband transitions in the Au nanoparticle are clarified.

DOI: [10.1103/PhysRevB.100.035446](https://doi.org/10.1103/PhysRevB.100.035446)

I. INTRODUCTION

Noble metal nanoparticles (NPs) exhibiting large optical nonlinearity and ultrafast response are considered promising materials in nanophotonics [1–3]. The localized surface plasmon resonance (LSPR), which originates from the coherent oscillation of conduction electrons near the metal NP's surface [4], can strongly enhance the nonlinear optical (NLO) response [2]. Note that the nanocomposites' effective third-order nonlinearity $\chi_{\text{composite}}^{(3)}$ is crucially influenced by geometric factors and intrinsic third-order nonlinearity $\chi_{\text{NP}}^{(3)}$ of the metal nanomaterials [5]. Thus, by tailoring the plasmon resonances, the NLO response of these metamaterials becomes very attractive for several long-awaited applications in nanophotonics, such as third-harmonic generation (THG), surface-enhanced Raman scattering (SERS), and ultrafast all-optical switching [6–8]. In these functionalities, Au plays an important role because of its large nonlinearity and chemical stability [9–11]. Au nanostructures simultaneously show photoinduced absorption and transparency depending on specific wavelength regions [12]. Due to the overlap of the plasmon resonance and interband transitions, it is suggested that the $\chi_{\text{Au composite}}^{(3)}$ exhibits a complex wavelength dependence

[13]. Furthermore, to the best of our knowledge, $\chi^{(3)}$ of Au nanostructures has only been reported at a few discrete wavelengths due to technical limitations [14]. These results have led to conflicting attributions to the underlying physical mechanisms, such as two-photon absorption [15], local field effects [16], interband transitions [17], Fermi smearing [18], and hot electrons [19]. To move the plasmonic materials toward real world applications, a better understanding of the spectral dependence is needed in order to control and enhance the ultrafast transient NLO response.

The NLO response of Au nanostructures reflects the intraband transitions of the conduction electrons and interband transitions from valence band to conduction band [2]. Several NLO studies have been carried out on these nanostructures using Z-scan techniques [14]. They have particularly analyzed single-wavelength photoinduced transparency and absorption also known as saturable absorption (SA) and reverse SA (RSA), respectively. By ignoring the coupling between the real and imaginary components, SA and RSA had been associated to negative and positive values of the imaginary component $\chi_{\text{Au}}^{(3)''}$, respectively [16,20]. For Au thin film, Smith *et al.* [20] and Boyd *et al.* [21] experimentally observed RSA and $\chi_{\text{Au bulk}}^{(3)}$ of $(-0.39 + 2.2i) \times 10^{-16} \text{ m}^2/\text{V}^2$ and $(-76.8 + 4.3i) \times 10^{-20} \text{ m}^2/\text{V}^2$ were obtained at 2.33 eV (532 nm) and 1.97 eV (630 nm), respectively. In contrast, Marini *et al.* [17] have predicted a strong wavelength-dependent $\chi^{(3)}$ with consecutive positive and negative peaks

*zhang.boyi@nims.go.jp

†takeda.yoshihiko@nims.go.jp

from 6.20 eV (200 nm) to 1.24 eV (1000 nm) using thermomodulation of the dielectric constant of Au. As for Au NPs, SA was reported at 532 nm with $\chi_{\text{Au composite}}^{(3)''}$ of $-8.96 \times 10^{-20} \text{ m}^2/\text{V}^2$ [16]. In Ref. [22] RSA was observed at 1.55 eV (800 nm). Wang *et al.* [22] studied the intensity-dependent reversal of the photoinduced response at 1.55 eV (800 nm). They ascribed the positive and negative signs of $\chi_{\text{Au composite}}^{(3)''}$ to the competition of SA and two-photon absorption. Smith *et al.* [16] studied the photoinduced response with several Au nanoparticles' concentration at 2.33 eV. They observed a reversal of the photoinduced response and ascribed the positive and negative signs of $\chi_{\text{Au composite}}^{(3)''}$ to local field effects. Thus, these fragmental results at a few wavelengths have led to conflicting underlying physical mechanisms of the NLO response of Au nanostructures.

In this work, we investigated the wavelength-dependent dispersion $\chi^{(3)}$ of the Au thin film and Au/PVA nanocomposite combining spectroscopic ellipsometry (SE) and pump and probe spectroscopy measurements. We successfully evaluated the real and imaginary components of the $\chi^{(3)}$ of Au nanostructures in a broad range (1.50–3.10 eV). More importantly, we evaluated the intrinsic $\chi_{\text{Au NP}}^{(3)}$ of the Au NP with Maxwell-Garnett effective medium approximation (EMA) and demonstrated the interband and intraband contributions. Conversely to Ag NP where the interband transitions and plasmon resonance are spectrally separated [23], Au NP exhibits a more complex spectral signature due to a partial overlap of the interband transitions with the plasmon resonance.

II. EXPERIMENT SETUP

A. Fabrication

Au thin film was deposited on a 0.5-mm amorphous SiO₂ silica glass substrate by magnetron sputtering using an Au target (99.99%) [24]. The base pressure in the deposition chamber was kept below 0.1 Pa. The thickness of 26 nm was controlled by deposition time.

Au NPs had been embedded in a poly(vinyl alcohol) (PVA) matrix by spin coating as previously reported in Ref. [25]. Au

NPs (Nanopartz Inc.) with average diameter size of 10 nm dispersed in water with optical density of 1.08 were used without any further treatment. They were separated from the mother liquid by centrifugation (13 000 RPM, 10 min, Harmony, MCF-1350). After centrifugation, 20 μl of the precipitated NPs was redispersed in 10 μl of PVA solution (20 g/l) and sonicated. The substrates used were the same SiO₂ substrates, which were precleaned by an ozone cleaner (Filgen, UV253). The substrates were vacuum locked during the spin-coating process (Mikasa, MS-A100) and a uniform coating with a thickness of about 600 nm was prepared at a spinning rate of 800 rpm for 10 min with 15 μl of the Au/PVA suspensions.

B. Measurement

The linear optical properties (phase and polarization changes of reflection, and also transmission intensity) of the Au thin film and the Au/PVA composite film were measured by spectroscopic ellipsometry (SE) (Woollam, VASE) from 1.24 to 3.10 eV (350–1000 nm) at incident angles of 50°, 60°, and 70°. The thickness and dielectric function ϵ were obtained from ellipsometric data analysis. For the Au thin film, ϵ_{Au} is summed by the Drude-Gaussian terms as below [26]:

$$\epsilon_{\text{Au}}(\omega) = \epsilon_{\text{Drude}}(\omega) + \sum \epsilon_{\text{Gaussian}}(\omega). \quad (1)$$

The Drude oscillator describes the free carrier absorption whose expression is given by [26]

$$\epsilon_{\text{Drude}}(\omega) = \frac{-1}{2\pi \epsilon_0 \rho (2\pi \tau \omega^2 + i\omega)}, \quad (2)$$

where ϵ_0 is vacuum dielectric constant, and ρ (resistivity) and τ (scattering time) are the fitting parameters for the Drude oscillator. Gaussian oscillators describe the interband transitions. As reported in [27], four Gaussian oscillators were applied to describe the interband transitions and can be written as [26]

$$\begin{aligned} \sum_1^4 \epsilon_{\text{Gaussian}}(\omega)_n &= \sum_1^4 \text{Amp}_n \left(\left[\Gamma \left(\frac{h\omega - h\omega n_n}{\sigma_n} \right) \right] + \left[\Gamma \left(\frac{h\omega + h\omega n_n}{\sigma_n} \right) \right] \right. \\ &\quad \left. + i \left\{ \exp \left[- \left(\frac{h\omega - h\omega n_n}{\sigma_n} \right)^2 \right] - \exp \left[- \left(\frac{h\omega + h\omega n_n}{\sigma_n} \right)^2 \right] \right\} \right), \\ \text{and } \sigma_n &= \frac{\text{Br}_n}{2\sqrt{\ln(2)}} \end{aligned} \quad (3)$$

where the function Γ stands for the Dawson function that produces a Kramers-Kronig consistent line shape for the real part and can be written as [28]

$$\Gamma(x) = \exp(-x^2) \int_0^x \exp(t^2) dt, \quad (4)$$

for which efficient numerical algorithms exist. Fitting parameters are Amp (amplitude), Br (broadening), and En (center

energy, which is defined by $h\omega n_n$). The Au/PVA composite was modeled using the Maxwell-Garnett EMA. The dielectric function of the PVA medium was described by a simple Cauchy equation obtained by analyzing a pure PVA thin film. ϵ_{Au} of the Au NPs was modeled by the Drude-Gaussian terms using Eqs. (1)–(3). Note that the four Gaussian oscillators are an approximation to model the band structure of Au [26]. The approximation cannot reproduce the finer structures because

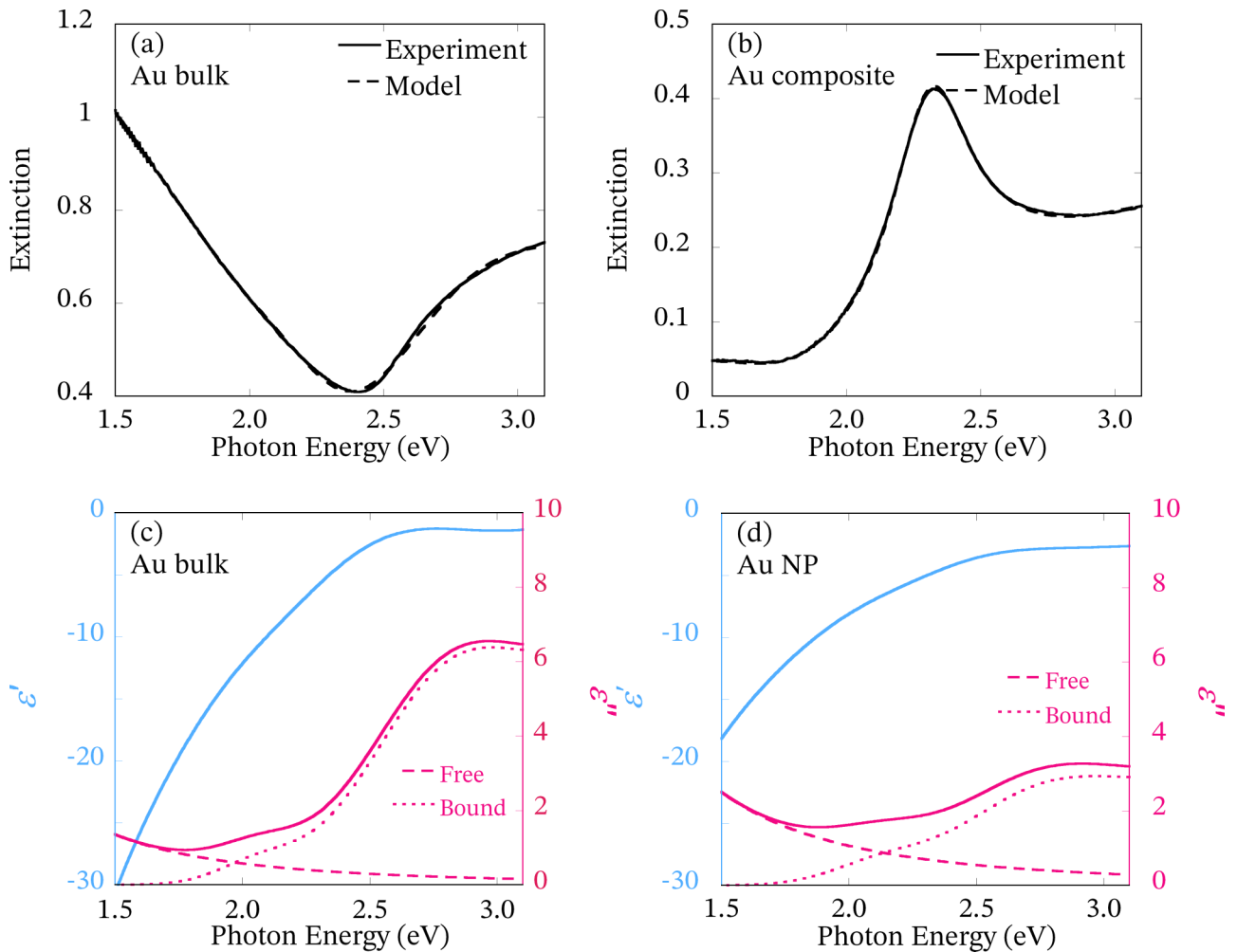


FIG. 1. Linear optical properties evaluated from spectroscopic ellipsometry. Measured (solid line) and extracted from SE model (dashed line) extinction spectra of the Au thin film (a) and Au/PVA composite (b). Linear dielectric function of the Au thin film (c) and Au NP (d): The continuous lines represent real (blue) and imaginary (red) components. The free and bound contributions to imaginary components are represented by dashed and dotted lines, respectively.

it would require additional oscillators, which may lead to an inaccurate SE model [29].

Figures 1(a) and 1(b) show the experimental and SE model fitted extinction of the thin film and Au/PVA composite, respectively. The minimized mean squared error (MSE) for ellipsometric fitting was 5.6 and 7.5 for thin film and Au/PVA composite, respectively. MSE between the SE model and experimental data is used to describe the fitting quality. For an ideal SE model, MSE would be around 1. As reported in Ref. [30], MSE up to 10 can be accurate enough to describe the linear optical properties. Figures 1(c) and 1(d) show the ϵ of the Au thin film and intrinsic Au NPs, respectively. Full lines indicate the total components of the ϵ , where the real and imaginary components were represented by blue and red lines, respectively. Dashed and dotted lines indicate the individual contributions of Drude (free electrons) and Gaussian (bound electrons) contributions to the imaginary component ϵ'' . The detailed parameters are shown in Table I. The Au thin film evaluated spectrum is well consistent with Johnson and Christy's bulk Au data [31]. In the case of Au NPs, we observed an increase (decrease) of the Drude term (Gaussian

terms) compared to the bulk Au. Similar differences between Au NPs and thin film were experimentally reported in other works [32,33]. Considering the obtained MSE values and compatibility of the dielectric functions of Au thin film and intrinsic NP with the literature, the obtained SE models can be considered adequate to describe their linear optical properties.

The photoinduced modulation was measured by pump and probe spectroscopy. The quantities measured are the transient transmission changes ($\Delta T/T$) and transient reflection changes ($\Delta R/R$). The laser source was supplied by a Ti:sapphire regenerative amplifier (Spitfire, Spectra-Physics) seeded with an oscillator (Mai Tai, Spectra-Physics) and pumped with a diode-pumped laser (Empower, Spectra-Physics) with an output pulse width of 130 fs at 1.55 eV (800 nm) and 1-kHz repetition rate. The fundamental laser beam was divided into two parts. One part, the pump beam, was converted into 3.10 eV (400 nm) generated by second-harmonic generation using a BBO crystal. The repetition rate was decreased to 0.5 kHz by an optical chopper and the peak intensity of the pump beam was set as 5.84 GW/cm² to avoid damage to the samples. The other part was converted into

TABLE I. Fitting parameters of the oscillators from spectroscopic ellipsometry model.

	Au thin film			Au NP		
	τ (fs)	ρ ($\times 10^{-6} \Omega \text{ cm}$)		τ (fs)	ρ ($\times 10^{-6} \Omega \text{ cm}$)	
Drude	12.68	4.38		3.74	26.79	
Gaussian	Amp	Br (eV)	En (eV)	Amp	Br (eV)	En (eV)
1	0.55	0.37	2.07	0.52	0.44	2.12
2	5.10	0.73	2.80	1.89	0.72	2.71
3	4.36	0.81	3.42	2.54	0.99	3.34
4	4.14	1.00	4.17	1.20	0.60	4.01
MSE	5.585			7.505		

the white-light supercontinuum as a probe beam which was generated by a CaF₂ crystal with a wide photon energy range 1.65 eV (350 nm) to 3.54 eV (750 nm). The chirping effect was measured and corrected by using the Kerr gate method [34]. The laser induced excitation and relaxation processes of electrons can be divided into four steps demonstrated by Voisin *et al.* [35] according to the smearing of electron distribution. First, the interband absorption takes place from the upper *d* band to the empty states above the Fermi level. Second, this absorption immediately leads to a strong athermal distribution of the electrons in the conduction band [36]. Third, the thermal redistribution takes place and, consequently, a broadening of the Fermi-Dirac electron distribution around the Fermi level [37]. The characterized thermalization time of bulk Au is ~ 500 fs. The start of redistribution is accompanied by the increase of $\Delta T/T$ and $\Delta R/R$ amplitude in pump-probe measurements. At this stage, we extracted the maximum amplitude of $\Delta T/T$ and $\Delta R/R$ for the evaluation of $\chi^{(3)}$. Finally, through the interaction of electron-phonon scattering, the energy is transferred to the lattice [35].

Combining pump-probe spectroscopy and spectroscopic ellipsometry measurements, the $\chi^{(3)}$ was evaluated as reported in Ref. [38]. Firstly, the transmission at excited state $T + \Delta T$ was calculated from the measured transient transmission changes based on the transmission at steady state from the SE model. Secondly, the dielectric function at excited state $\varepsilon + \Delta\varepsilon$ was extracted by fitting optical oscillators' parameters of the linear SE model to the $T + \Delta T$ while keeping other structural parameters (thickness, volume fraction, and so on) the same. We kept the Drude parameters the same for the Au thin film. The free electrons' contribution is ignored in this way following the same considerations as in previous works

in the literature [39]. The fitted oscillator parameters and MSE are listed in Table II. The photoinduced dielectric function modulation $\Delta\varepsilon$ was extracted from the difference of excited state $\varepsilon + \Delta\varepsilon$ and steady state ε . $\Delta\varepsilon$ is proportional to the $\chi^{(3)}$ and the converting formulas were reported in Ref. [40].

III. RESULTS AND DISCUSSION

A. Thin film

To study the nonlinear optical properties of the bulk Au, the measurements of $\Delta T/T$ and $\Delta R/R$ were performed and displayed in Fig. 2(a). Note that the peak located at 3.10 eV is due to scattering of the pump light. The $\Delta T/T$ spectrum includes regions of a strong positive peak (center) and two negative peaks (wings). The positive and negative $\Delta T/T$ values are attributed to photoinduced transparency and absorption, respectively [12]. The maximum intensity of the induced absorption peak is located at 2.45 eV inside the linear transmission window, which is defined between the threshold of interband absorption and the onset of the long-wavelength reflection [20]. The $\Delta R/R$ spectrum contains regions of photoinduced reflection (center) and reversed photoinduced reflection (wings). Near the transmission window, the maximum intensity of the induced reflection peak is located at 2.50 eV.

The dielectric function at the excited state $\varepsilon + \Delta\varepsilon$ was extracted using the transmission at the excited state $T + \Delta T$ similarly to Ref. [38]. The respective $\Delta T/T$ from the SE model was plotted in Fig. 2(a). Throughout the paper, the third-order susceptibility of the bulk Au is expressed as $\chi_{\text{Au bulk}}^{(3)}$ and extracted from $\Delta\varepsilon$ as reported in Ref. [40]:

$$\Delta\varepsilon(\omega_{\text{probe}}) = \frac{3}{4}\chi_{\text{Au bulk}}^{(3)}(\omega_{\text{probe}})I, \quad (5)$$

TABLE II. Oscillator parameters at excited states.

	Au thin film			Au NP		
	τ (fs)	ρ ($\times 10^{-6} \Omega \text{ cm}$)		τ (fs)	ρ ($\times 10^{-6} \Omega \text{ cm}$)	
Drude	12.68	4.38		3.72	26.80	
Gaussian	Amp	Br (eV)	En (eV)	Amp	Br (eV)	En (eV)
1	0.34	0.32	2.03	0.63	0.49	2.10
2	5.85	1.00	2.92	1.81	0.71	2.65
3	3.69	0.75	3.63	2.60	0.96	3.30
4	5.80	0.86	4.25	1.48	0.68	3.99
MSE	4.595			2.780		

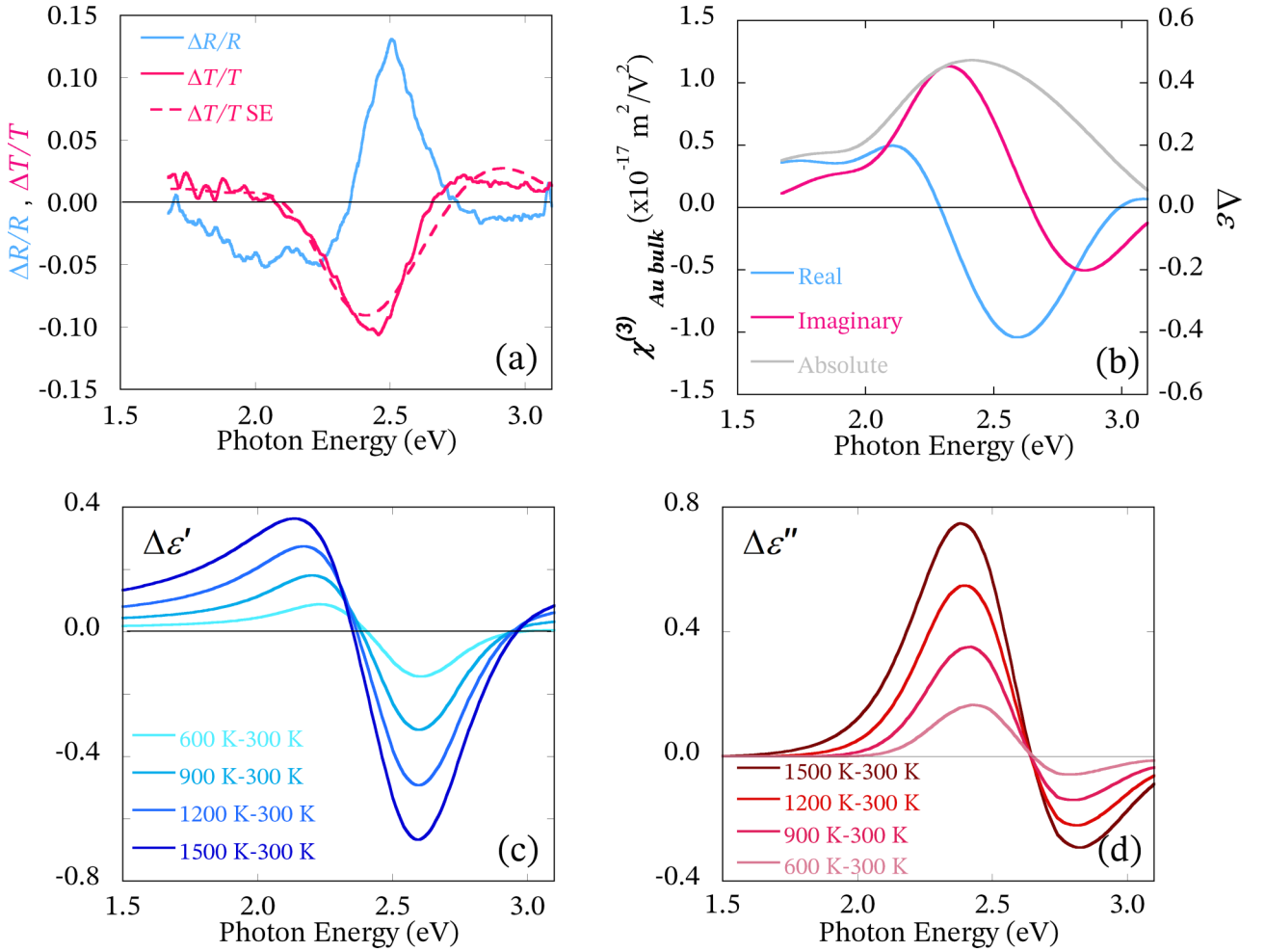


FIG. 2. (a) Spectral dependence of transient reflection (blue) and transmission (red) changes of the bulk Au. The red dashed line represents the transient transmission changes extracted from the SE model. (b) Third-order susceptibility $\chi_{Au\ bulk}^{(3)}$ and corresponding dielectric function modulation $\Delta\varepsilon$ as a function of photon energy: Blue, red, and gray curves correspond to the real, imaginary, and absolute components, respectively. Calculated real (c) and imaginary (d) components of $\Delta\varepsilon(\omega)_{bound}$ of the Au bulk (with an offset): The shades of the color represent different equivalent electron temperature varying from 600 to 1500 K.

where $\frac{3}{4}$ is the K factor for intensity-dependent refractive index [41] and I the pump laser intensity. The real and imaginary components of the $\chi_{Au\ bulk}^{(3)}$ and $\Delta\varepsilon$ are shown in Fig. 2(b). Both real $\chi_{Au\ bulk}^{(3)'}$ and imaginary $\chi_{Au\ bulk}^{(3)''}$ components show a strong wavelength-dependent dispersion consisting of a positive peak following a small negative peak, which cannot be simply described and understood by single-wavelength measurements. The maximum positive peak of $\chi_{Au\ bulk}^{(3)'}$ is located inside the transmission window at 2.34 eV with a magnitude of $1.19 \times 10^{-17} \text{ m}^2/\text{V}^2$, and reflects the strong photoinduced absorption in $\Delta T/T$. The peaks at lower and higher energies reflect the photoinduced transparency. The minimum of $\chi_{Au\ bulk}^{(3)'}$ of $-1.11 \times 10^{-17} \text{ m}^2/\text{V}^2$ is located at 2.58 eV.

It is well accepted that interband transitions play a dominant role for the nonlinearity of bulk Au. The initial theoretical and experimental results were reported by Guerrisi and Rosei *et al.* [39,42], where they reported the thermomodulation reflection contributed from interband transitions at the X

and L points. Recently, Conforti and Della Valle [43], and Marini *et al.* [17] have reported the derivation of $\chi_{Au\ bulk}^{(3)}$ from Rosei's model, which is known as thermomodulation interband nonlinear susceptibility. Although the theoretical description of the thermomodulation $\chi_{Au\ bulk}^{(3)}$ has been done, a comparison between $\chi_{Au\ bulk}^{(3)}$ and respective ΔT is still missing. Here we applied a simplified model to calculate the dielectric function modulation. Then, combining with the SE model, $\chi_{Au\ bulk}^{(3)}$ and its respective ΔT were extracted. In detail, we had carried out a density-functional theory (DFT) calculation of the dielectric function modulation of Au bulk, which is rooted in quantum calculations [44]. The following calculation considers the induced modifications of the interband contribution to the dielectric function and is denoted as $\varepsilon(\omega)_{bound}$. The band structure of Au was calculated by DFT and generalized gradient approximation with the plane-wave pseudopotential method [45–48]. $\varepsilon(\omega)_{bound}$ was calculated using a $36 \times 36 \times 36$ k -point mesh and a number of bands of 32. The real and imaginary components of $\varepsilon(\omega)_{bound}$ were

numerically calculated with the Fermi-Dirac distribution at each electronic temperature as

$$\varepsilon_{\alpha\beta}(\omega)''_{\text{bound}} = \frac{8\pi^2 e^2}{m_e^2 \omega^2 V} \sum_{k,i,j} p_{ji,\alpha}^k p_{ij,\beta}^k f(E_i^k) \times [1 - f(E_j^k)] \delta(E_j^k - E_i^k - \hbar\omega), \quad (6)$$

$$\varepsilon_{\alpha\beta}(\omega)'_{\text{bound}} = 1 + \frac{2}{\pi} P \int_0^\infty \frac{\omega' \varepsilon_{\alpha\beta}(\omega')''_{\text{Au}}}{\omega'^2 - \omega^2} d\omega', \quad (7)$$

where m_e and V represent the mass of electrons and unit cell volume, respectively; $p_{ij,\alpha}^k = \langle \varphi_j^k | p_\alpha | \varphi_i^k \rangle$ express a certain transition moment between each wave function, φ_j^k , of the j th band at k ; $f(E_i^k)$ is the Fermi-Dirac distribution with an energy, E_i^k . α and β are the Cartesian indices (x , y , z) [49–51]. $\varepsilon(\omega)'_{\text{bound}}$ was evaluated from the Kramers-Kronig relation by using Eq. (5). $\Delta\varepsilon(\omega)_{\text{bound}}$ was calculated by the difference of $\varepsilon(\omega)_{\text{bound}}$ at two different electron temperatures:

$$\Delta\varepsilon(\omega)_{\text{bound}} = \varepsilon(\omega)_{\text{bound,excited}} - \varepsilon(\omega)_{\text{bound,steady}}. \quad (8)$$

The steady-state temperature for electrons was set at 300 K. To represent different pumping intensities, the electron temperatures at excited states were chosen from 600 to 1500 K. Owing to the minor difference of energy level between the model and the actual band structure, the photon energy of $\Delta\varepsilon(\omega)_{\text{bound}}$ included offset. The lattice temperature was set as 0 K. The calculated real and imaginary components of $\Delta\varepsilon(\omega)_{\text{bound}}$ are shown in Figs. 2(c) and 2(d). Note that the overall intensity of the $\Delta\varepsilon(\omega)_{\text{bound}}$ depends on the electrons' temperature; however, the spectrum profile remains the same. The real component of $\Delta\varepsilon(\omega)_{\text{bound}}$ contains a strong negative peak at 2.60 eV with two positive peaks at the wings. The imaginary component of $\Delta\varepsilon(\omega)_{\text{bound}}$ exhibits a strong positive peak at 2.38 eV with a following small negative peak at higher photon energy. The dispersion of $\Delta\varepsilon(\omega)_{\text{bound}}$ from our DFT model is similar to the calculation reported by Marini *et al.* [17]. Combining with the SE model, the transient transmission change ΔT was extracted from its respective $\Delta\varepsilon(\omega)_{\text{bound}}$ at a different electron temperature. For comparison, the calculated ΔT was plotted together with experimental data in Fig. 3 and the electron temperature was set as 1200 K to match the experimental amplitude [Fig. 2(b)]. Shown in Fig. 3, $\Delta T/T$ extracted from the DFT model consists of a strong photoinduced absorption at 2.45 eV and two photoinduced transparencies at the wings. The dispersion and amplitude from DFT calculation show an overall agreement of our experimental data. In addition, the DFT model is compatible with previous calculations reported by Conforti and Della Valle [43] and Marini *et al.* [17]. Thus, the contribution from interband transitions is suggested to play a dominant role in the nonlinear optical properties of bulk Au.

B. Nanoparticles

The $\Delta T/T$ of the Au/PVA composite was measured and is shown in Fig. 4(a). Compared to the bulk Au [Fig. 2(a)], one can observe that the dispersion of the Au/PVA composite is exceptionally different. The sharp positive peak (photoinduced transparency) is located at the plasmon resonance

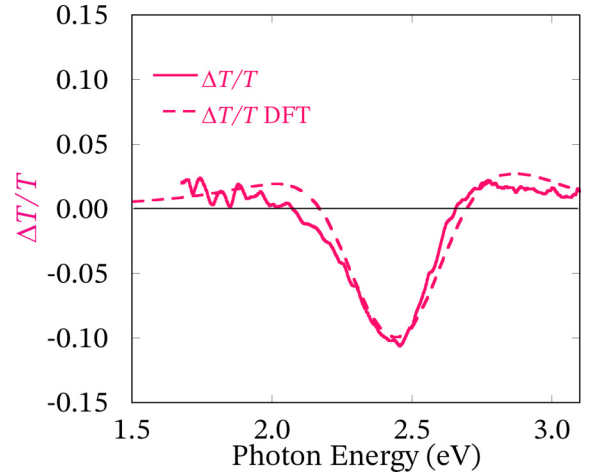


FIG. 3. $\Delta T/T$ extracted from DFT calculation by the SE model (dotted line). The electron temperature was selected as 1200 K. The solid line is the experimental data from pump and probe spectroscopy, extracted from Fig. 2(a).

(2.32 eV) of the Au NP. At the wings of photoinduced transparency, weaker photoinduced absorption peaks are observed. Interestingly, at higher photon energy away from the plasmon resonance, the $\Delta T/T$ shows opposite sign compared to the bulk Au. This difference indicates that the interaction between the LSPR and interband transition at the nonlinear state is complex instead of a simple summation. Note that the $\Delta R/R$ signal was too weak to be detected. The effective third-order susceptibility of the Au/PVA composite $\chi_{\text{Au composite}}^{(3)}$ was evaluated using Eq. (5) and is shown in Fig. 4(b). The imaginary part comprises, successively, positive, negative, and positive peaks, which reflect the photoinduced transparency at plasmon resonance and the photoinduced absorption at the wings. The minimum value is $-9.62 \times 10^{-19} \text{ m}^2/\text{V}^2$ at 2.32 eV. The minimum intensity of the real component is $-6.58 \times 10^{-19} \text{ m}^2/\text{V}^2$ at 2.21 eV. The strongest peak of these two components both locates around LSPR and decays towards the two wings.

As suggested by the Maxwell-Garnett EMA, the NLO properties of the Au/PVA composite are strongly influenced by the intrinsic nonlinearities of metals and the surrounding dielectric environments. Thus, it is important to evaluate the intrinsic third-order susceptibility of the Au NP $\chi_{\text{Au NP}}^{(3)}$ to understand the macroscopic nonlinearity. The $\chi_{\text{Au NP}}^{(3)}$ was evaluated from the dielectric function modulation of the Au NP $\Delta\varepsilon_{\text{Au NP}}$ similarly to Ref. [38] and was expressed as

$$\Delta\varepsilon_{\text{Au NP}}(\omega_{\text{probe}}) = \frac{3}{4} \chi_{\text{Au NP}}^{(3)}(\omega_{\text{probe}}) |f_l(\omega_{\text{pump}})|^2 I, \quad (9)$$

where $f_l(\omega_{\text{pump}})$ is the local field enhancement factor at the photon energy of the pump excitation, which is defined as the ratio of the local field to the applied one. $f_l(\omega)$ is calculated by the dielectric function of Au and PVA matrix as $f_l(\omega) = \frac{3\varepsilon_{\text{PVA}}}{\varepsilon_{\text{Au NP}} + 2\varepsilon_{\text{PVA}}}$. The real and imaginary components of the $\chi_{\text{Au NP}}^{(3)}$ reflect the photoinduced modulation of the interband and intraband transitions and are shown in Fig. 4(c). The $\chi_{\text{Au NP}}^{(3)''}$ consists of a broad positive peak with maximum intensity of $\chi_{\text{Au NP}}^{(3)''} 1.25 \times 10^{-17} \text{ m}^2/\text{V}^2$ near the transmission window and a small negative peak at higher photon energy. The dispersion

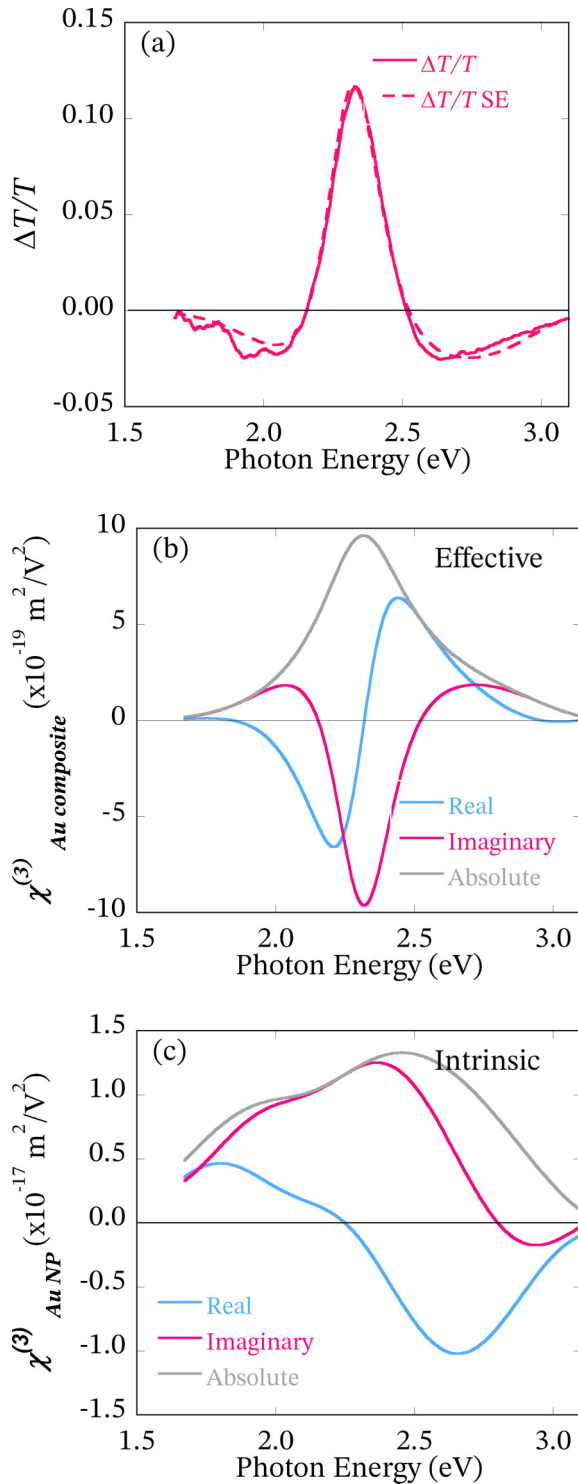


FIG. 4. (a) $\Delta T/T$ of PVA/Au composite from experimental measurements (solid line) and the SE model (dashed line); (b) macroscopic third-order susceptibility $\chi_{Au\ composite}^{(3)}$; (c) intrinsic third-order susceptibility $\chi_{Au\ NP}^{(3)}$: Blue, red, and gray curves correspond to the real, imaginary, and absolute components, respectively.

of $\chi_{Au\ NP}^{(3)}$ shows a similar structure to $\chi_{Au\ bulk}^{(3)}$: a strong peak centered at the edge of the interband transitions with small peaks at the wings. However, the difference at lower photon energy suggests extra contributions need to be considered.

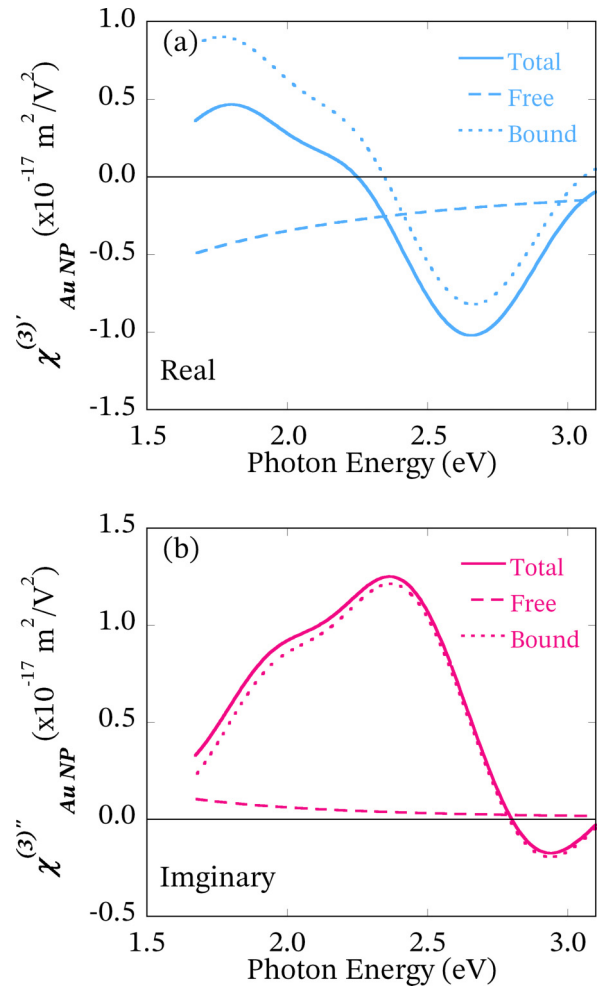


FIG. 5. Real (a) and imaginary (b) components of the intrinsic third-order susceptibility $\chi_{Au\ NP}^{(3)}$: The free electrons' contribution was evaluated from the Drude oscillator and is represented by the dashed line. The bound electrons' contribution was evaluated from the Gaussian oscillators and is represented by the dotted line. The solid line is $\chi_{Au\ NP}^{(3)}$ extracted from Fig. 3(c).

To understand how the interband and intraband transitions interact with each other at the nonlinear state, the contributions of the Drude term and Gaussian terms were separated and are shown in Fig. 5. The Drude term describes the intraband contribution and is denoted as $\chi_{Au\ NP\ free}^{(3)}$ (dashed line) and the Gaussian terms describe the interband contribution and are denoted as $\chi_{Au\ NP\ bound}^{(3)}$ (dotted line). As previously discussed, without the LSPR, the underlying mechanism of the optical nonlinearity of Au bulk is attributed to the interband transitions. For an Au NP, the interband contribution is equivalent to the Au bulk [Fig. 2(b)] while exhibiting a broader dispersion originating from the linear dielectric function. Using time-dependent DFT, He and Zeng [52] predicted a convergence of the interband contribution of an Au NP to bulk for particles with a radius larger than 1–2 nm. The intraband contribution also plays an important role due to an increase of the electron collision rate (see $\chi_{Au\ NP\ free}^{(3)}$ in Fig. 5) [52]. The $\chi_{Au\ NP\ free}^{(3) \prime \prime}$ exhibits a monotonic dispersion decreasing towards higher photon energy. Although we carefully examined the Au/PVA composite and compared it to Au

bulk to properly separate these contributions, note that their interplay at the nonlinear state is complex. In the literature [12,52,53], some authors explained the NLO response of metal NPs as interband transitions while others stated it originates from the intraband transitions. However, both contributions are necessary to explain the intrinsic optical nonlinearity of the Au NP in the visible region.

Summarizing these arguments, we have experimentally investigated the $\chi_{\text{Au bulk}}^{(3)}$ and macroscopic $\chi_{\text{Au composite}}^{(3\text{eqn}3)}$ and intrinsic $\chi_{\text{Au NP}}^{(3)}$ in a broad photon energy (1.50–3.10 eV). Firstly, we have demonstrated the wavelength-dependent behavior of the transient transmission changes of the Au bulk and NPs. Through this result, we clarified that SA and RSA can be simultaneously observed at different photon energies. Secondly, the evaluated real components of $\chi_{\text{Au bulk}}^{(3)}$, $\chi_{\text{Au composite}}^{(3)}$, and $\chi_{\text{Au NP}}^{(3)}$ exhibited similar amplitude to the imaginary components at different photon energy. However, single-wavelength Z-scan results, particularly at 532 nm, led to a conclusion that $\chi_{\text{Au}}^{(3)''}$ can be much weaker than $\chi_{\text{Au}}^{(3)'}$ [20] or simply ignored [54]. Thirdly, and most importantly, we clarified the physical mechanism of the NLO response of Au nanostructures. Through the calculation and experiments on the Au thin film, we discussed the interband contribution to the dispersion of the $\chi_{\text{Au bulk}}^{(3)}$ in detail. In the case of Au NPs, interband and intraband contributions must be taken into consideration. We untangled that the $\chi_{\text{Au NP free}}^{(3)}$

shows a monotonic dispersion while $\chi_{\text{Au NP bound}}^{(3)}$ exhibits a wavelength-dependent dispersion from interband transitions. In this way, to design new nanostructures for future nanophotonic applications, the strong wavelength dependence and differences in the intrinsic nonlinearity of the nanostructures compared to the bulk materials should be taken into consideration.

IV. CONCLUSION

The dispersions of the third-order susceptibility were investigated by combined analysis with spectroscopic ellipsometry and pump and probe spectroscopy. We experimentally evaluated the $\chi_{\text{Au bulk}}^{(3)}$ of an Au thin film and $\chi_{\text{Au NP}}^{(3)}$ of an Au NP in a broad range (1.50–3.10 eV). These dispersions show a strong wavelength dependence and consist of several successively positive and negative peaks, which reflects the photoinduced electron distribution modulation. Also, the real and imaginary components exhibit a similar overall intensity. For Au bulk, as expected, the contribution from interband transitions dominates the third-order optical nonlinearity. For the Au/PVA composite, interband transitions and the LSPR contribute to the macroscopic nonlinearity. In addition, we clarified the individual contribution of the intraband and interband transitions to the intrinsic third-order nonlinearity of an Au NP.

-
- [1] M. S. Tame, K. R. McEnery, Ş. K. Özdemir, J. Lee, S. A. Maier, and M. S. Kim, *Nat. Phys.* **9**, 329 (2013).
- [2] M. Kauranen and A. V. Zayats, *Nat. Photonics* **6**, 737 (2012).
- [3] A. L. Stepanov, *Rev. Adv. Mater. Sci.* **27**, 115 (2011).
- [4] E. Hutter and J. H. Fendler, *Adv. Mater.* **16**, 1685 (2004).
- [5] J. E. Sipe and R. W. Boyd, *Phys. Rev. A* **46**, 1614 (1992).
- [6] A. Wokaun, J. G. Bergman, J. P. Heritage, A. M. Glass, P. F. Liao, and D. H. Olson, *Phys. Rev. B* **24**, 849 (1981).
- [7] S. L. Smitha, K. G. Gopchandran, T. R. Ravindran, and V. S. Prasad, *Nanotechnology* **22**, 265705 (2011).
- [8] R. Frank, *Phys. Rev. B* **85**, 195463 (2012).
- [9] S. K. Ghosh and T. Pal, *Chem. Rev.* **107**, 4797 (2007).
- [10] C. Sönnichsen, B. M. Reinhard, J. Liphardt, and A. P. Alivisatos, *Nat. Biotechnol.* **23**, 741 (2005).
- [11] L. Wu, H. S. Chu, W. S. Koh, and E. P. Li, *Opt. Express* **18**, 14395 (2010).
- [12] X. Wang, Y. Guillet, P. R. Selvakannan, H. Remita, and B. Palpant, *J. Phys. Chem. C* **119**, 7416 (2015).
- [13] D. Compton, L. Cornish, and E. van der Lingen, *Gold Bull.* **36**, 10 (2003).
- [14] M. Sheik-Bahae, A. A. Said, T. H. Wei, D. J. Hagan, and E. W. Van Stryland, *IEEE J. Quantum Electron.* **26**, 760 (1990).
- [15] M. Ren, B. Jia, J. Y. Ou, E. Plum, J. Zhang, K. F. MacDonald, A. E. Nikolaenko, J. Xu, M. Gu, and N. I. Zheludev, *Adv. Mater.* **23**, 5540 (2011).
- [16] D. D. Smith, G. Fischer, R. W. Boyd, and D. A. Gregory, *J. Opt. Soc. Am. B* **14**, 1625 (1997).
- [17] A. Marini, M. Conforti, G. Della Valle, H. W. Lee, T. X. Tran, W. Chang, M. A. Schmidt, S. Longhi, P. St. J. Russell, and F. Biancalana, *New J. Phys.* **15**, 013033 (2013).
- [18] F. Hache, D. Ricard, C. Flytzanis, and U. Kreibig, *Appl. Phys. A: Solids Surf.* **47**, 347 (1988).
- [19] S. D. Brorson, J. G. Fujimoto, and E. P. Ippen, *Phys. Rev. Lett.* **59**, 1962 (1987).
- [20] D. D. Smith, Y. Yoon, R. W. Boyd, J. K. Campbell, L. A. Baker, R. M. Crooks, and M. George, *J. Appl. Phys.* **86**, 6200 (1999).
- [21] R. W. Boyd, Z. Shi, and I. De Leon, *Opt. Commun.* **326**, 74 (2014).
- [22] K. Wang, H. Long, M. Fu, G. Yang, and P. Lu, *Opt. Lett.* **35**, 1560 (2010).
- [23] T. Stoll, P. Maioli, A. Crut, N. Del Fatti, and F. Vallée, *Eur. Phys. J. B* **87**, 260 (2014).
- [24] E. Xenogiannopoulou, P. Aloukos, S. Couris, E. Kaminska, A. Piotrowska, and E. Dynowska, *Opt. Commun.* **275**, 217 (2007).
- [25] R. Sato, S. Ishii, T. Nagao, M. Naito, and Y. Takeda, *ACS Photonics* **5**, 3452 (2018).
- [26] H. Fujiwara, *Spectroscopic Ellipsometry: Principles and Applications* (Wiley, New York, 2007).
- [27] A. D. Rakić, A. B. Djurišić, J. M. Elazar, and M. L. Majewski, *Appl. Opt.* **37**, 5271 (1998).
- [28] D. De Sousa Meneses, M. Malki, and P. Echegut, *J. Non-Cryst. Solids* **352**, 769 (2006).
- [29] J. N. Hilfiker, N. Singh, T. Tiwald, D. Convey, S. M. Smith, J. H. Baker, and H. G. Tompkins, *Thin Solid Films* **516**, 7979 (2008).
- [30] Z. Song, B. R. Rogers, and N. D. Theodore, *J. Vac. Sci. Technol. A* **22**, 711 (2004).
- [31] P. B. Johnson and R. W. Christy, *Phys. Rev. B* **6**, 4370 (1972).
- [32] D. Dalacu and L. Martinu, *J. Appl. Phys.* **87**, 228 (2000).
- [33] M. Quinten, *Z. Phys. B: Condens. Matter* **101**, 211 (1996).

- [34] W. Tan, H. Liu, J. Si, and X. Hou, *Appl. Phys. Lett.* **93**, 051109 (2008).
- [35] C. Voisin, N. Del Fatti, D. Christofilos, and F. Vallée, *J. Phys. Chem. B* **105**, 2264 (2001).
- [36] C.-K. Sun, F. Vallée, L. H. Acioli, E. P. Ippen, and J. G. Fujimoto, *Phys. Rev. B* **50**, 15337 (1994).
- [37] N. Del Fatti, C. Voisin, M. Achermann, S. Tzortzakis, D. Christofilos, and F. Vallée, *Phys. Rev. B* **61**, 16956 (2000).
- [38] R. Sato, M. Ohnuma, K. Oyoshi, and Y. Takeda, *Phys. Rev. B* **90**, 125417 (2014).
- [39] P. Winsemius, M. Guerrisi, and R. Rosei, *Phys. Rev. B* **12**, 4570 (1975).
- [40] Y. Takeda, O. A. Plaksin, and N. Kishimoto, *Opt. Express* **15**, 6010 (2007).
- [41] P. N. Butcher and D. Cotter, *The Elements of Nonlinear Optics* (Cambridge University Press, Cambridge, UK, 1990).
- [42] R. Rosei and D. W. Lynch, *Phys. Rev. B* **5**, 3883 (1972).
- [43] M. Conforti and G. Della Valle, *Phys. Rev. B* **85**, 245423 (2012).
- [44] Y. Takeda, H. Momida, M. Ohnuma, T. Ohno, and N. Kishimoto, *Opt. Express* **16**, 7471 (2008).
- [45] P. Hohenberg and W. Kohn, *Phys. Rev.* **136**, B864 (1964).
- [46] W. Kohn and L. J. Sham, *Phys. Rev.* **140**, A1133 (1965).
- [47] J. P. Perdew, K. Burke, and M. Ernzerhof, *Phys. Rev. Lett.* **77**, 3865 (1996).
- [48] D. Vanderbilt, *Phys. Rev. B* **41**, 7892 (1990).
- [49] H. Momida, T. Hamada, and T. Ohno, *Jpn. J. Appl. Phys.* **46**, 3255 (2007).
- [50] H. Momida, T. Hamada, Y. Takagi, T. Yamamoto, T. Uda, and T. Ohno, *Phys. Rev. B* **75**, 195105 (2007).
- [51] H. Kageshima and K. Shiraishi, *Phys. Rev. B* **56**, 14985 (1997).
- [52] Y. He and T. Zeng, *J. Phys. Chem. C* **114**, 18023 (2010).
- [53] M. Perner, P. Bost, U. Lemmer, G. von Plessen, J. Feldmann, U. Becker, M. Mennig, M. Schmitt, and H. Schmidt, *Phys. Rev. Lett.* **78**, 2192 (1997).
- [54] S. Debrus, J. Lafait, M. May, N. Pinçon, D. Prot, C. Sella, and J. Venturini, *J. Appl. Phys.* **88**, 4469 (2000).